

# Rapid Wafer-Scale Growth of Polycrystalline 2H-MoS<sub>2</sub> by Pulsed Metal–Organic Chemical Vapor Deposition

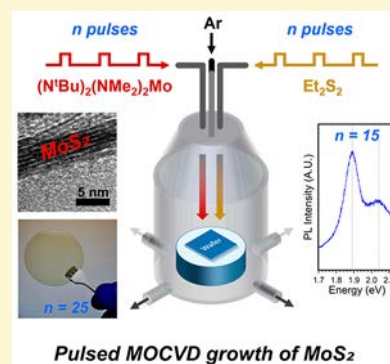
Berc Kalanyan,<sup>\*,†</sup> William A. Kimes,<sup>†</sup> Ryan Beams,<sup>†</sup> Stephan J. Stranick,<sup>†</sup> Elias Garratt,<sup>†</sup> Irina Kalish,<sup>†</sup> Albert V. Davydov,<sup>†</sup> Ravindra K. Kanjolia,<sup>‡</sup> and James E. Maslar<sup>†</sup>

<sup>†</sup>Material Measurement Laboratory, National Institute of Standards and Technology, Gaithersburg, Maryland 20899, United States

<sup>‡</sup>EMD Performance Materials, Haverhill, Massachusetts 01835, United States

## Supporting Information

**ABSTRACT:** High-volume manufacturing of devices based on transition metal dichalcogenide (TMD) ultrathin films will require deposition techniques that are capable of reproducible wafer-scale growth with monolayer control. To date, TMD growth efforts have largely relied upon sublimation and transport of solid precursors with minimal control over vapor-phase flux and gas-phase chemistry, which are critical for scaling up laboratory processes to manufacturing settings. To address these issues, we report a new pulsed metal–organic chemical vapor deposition (MOCVD) route for MoS<sub>2</sub> film growth in a research-grade single-wafer reactor. Using bis(*tert*-butylimido)-bis(dimethylamido)molybdenum and diethyl disulfide, we deposit MoS<sub>2</sub> films from ~1 nm to ~25 nm in thickness on SiO<sub>2</sub>/Si substrates. We show that layered 2H-MoS<sub>2</sub> can be produced at comparatively low reaction temperatures of 591 °C at short deposition times, approximately 90 s for few-layer films. In addition to the growth studies performed on SiO<sub>2</sub>/Si, films with wafer-level uniformity are demonstrated on 50 mm quartz wafers. Process chemistry and impurity incorporation from precursors are also discussed. This low-temperature and fast process highlights the opportunities presented by metal–organic reagents in the controlled synthesis of TMDs.



## 1. INTRODUCTION

Layered two-dimensional (2D) transition-metal dichalcogenides (TMDs), such as MoS<sub>2</sub>, WSe<sub>2</sub>, and ReS<sub>2</sub>, are of increasing interest for next-generation nanoelectronic and optoelectronic devices due to their unique thickness-modulated electronic properties.<sup>1</sup> When structured into single or few atomic layers, some TMDs develop a direct band gap due to quantum confinement,<sup>2</sup> which enables their use in low-power field-effect transistor (FET) devices.<sup>3–5</sup> In addition to traditional logic devices, structures consisting of TMDs are also being investigated for use in valleytronics,<sup>6</sup> memory applications,<sup>7</sup> chemical sensing,<sup>8,9</sup> optoelectronics,<sup>10–12</sup> energy devices,<sup>13</sup> and life sciences.<sup>14,15</sup> When assembled into van der Waals heterostructures with TMDs or other 2D materials (graphene, hexagonal boron nitride, etc.), novel and unique device arrangements<sup>16,17</sup> become realizable without the need for epitaxial matching between the layers. Furthermore, incorporation of dopants into TMDs,<sup>18–21</sup> alloying of various layered compounds,<sup>22</sup> and heterojunction assemblies<sup>23–25</sup> highlight the immense level of tunability afforded by layered 2D systems. Despite their tremendous potential for new applications, synthetic routes available for 2D TMDs have been largely limited to growth techniques that are difficult to scale, have low throughput, or do not offer sufficient control over the process chemistry to achieve reproducible material properties. Additionally, commonly employed powder vaporization routes, such as MoS<sub>2</sub> from MoO<sub>3</sub> and S, require high growth temperatures

and are not suitable for downstream integration with existing electronic manufacturing process flows.

Synthetic high-quality bulk TMD crystals are commonly produced by the chemical vapor transport method.<sup>26</sup> After growth, individual layers held together by van der Waals forces can be separated from the bulk by mechanical exfoliation and transferred onto device substrates. Although this approach is successful for small-scale device development and fundamental studies, large-area growth of TMDs requires vapor-phase deposition routes. The simplest approach that employs vapor-phase reagents is direct chalcogenization of metal foils<sup>27,28</sup> or thin films.<sup>29</sup> These approaches pose several challenges, particularly in terms of compatibility with semiconductor process flows and 3D integration. For instance, growth on sacrificial substrates requires the mechanical transfer of TMDs onto a target substrate, and metal chalcogenization requires a separate metal deposition step. Among other growth techniques, powder vaporization in flow tube reactors using inorganic sources such as transition metal oxides and elemental chalcogens have been widely used to produce a variety of 2D TMDs.<sup>30–34</sup> While high-quality films are routinely produced in this manner, the inherent lack of control over precursor flux and the process variability associated with flow tube geometry severely limit the scalability of powder vaporization. Even with

Received: April 3, 2017

Revised: July 9, 2017

Published: July 12, 2017

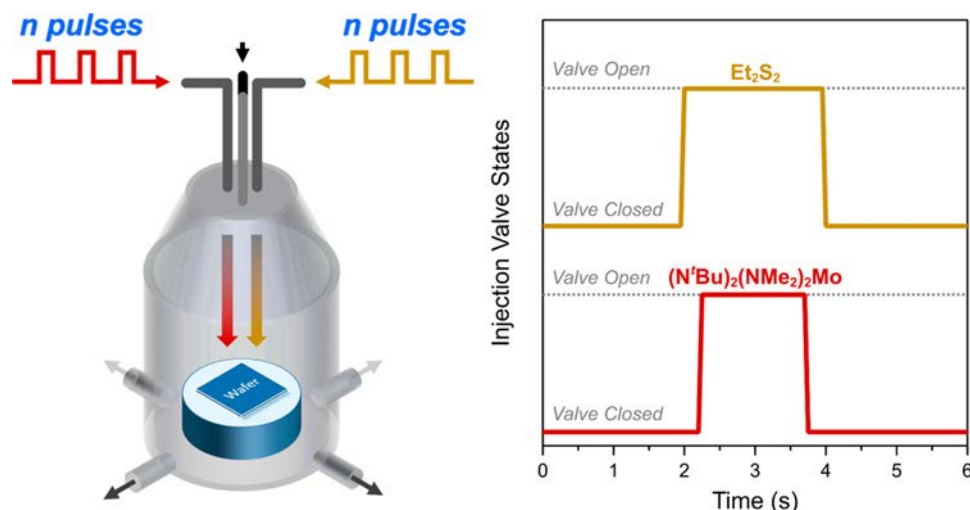


**Figure 1.** Overview of pulsed MOCVD process. (Left) Schematic of reactor geometry; (right) injection sequence of Mo and S precursors in a 6 s period.

high vapor pressure precursors, hot-walled flow tube reactors present problems with parasitic wall reactions, that is, partial conversion of precursors before they reach the substrate.

To overcome scalability and process control issues, recent reports on TMD synthesis have focused on using alternative metal precursors, primarily transition metal halides<sup>35</sup> such as  $\text{MoCl}_5$  or metal carbonyls<sup>36</sup> such as  $\text{Mo}(\text{CO})_6$ . Halides have also been used in low-temperature processes, with several examples of atomic layer deposition (ALD)<sup>37,38</sup> reported to date. At low growth temperatures, ALD TMD routes do not produce crystalline material and corrosive reaction products are generally undesirable. Recently, a new chemical vapor deposition (CVD) route was proposed by Robinson and co-workers,<sup>39</sup> using  $\text{W}(\text{CO})_6$ ,  $(\text{CH}_3)_2\text{Se}$ , and  $\text{H}_2$  to produce large-grain  $\text{WSe}_2$ . Using an analogous chemistry, Kang et al.<sup>36</sup> found that layer-by-layer or 2D growth of  $\text{MoS}_2$  occurred in a tube reactor under sufficiently low  $\text{Mo}(\text{CO})_6$  flux, which necessitated extremely long growth times of 26 h per monolayer  $\text{MoS}_2$ . Metal carbonyls are typically used for low-temperature metal CVD reactions due to their zerovalent state.<sup>40</sup> However, high reaction temperatures (typically 800–900 °C) needed to produce large-grain TMDs pose unique challenges for transition metal carbonyl sources. Iron and nickel carbonyls are known to form<sup>41</sup> readily upon reaction of CO and  $\text{H}_2$  with exposed stainless steel surfaces (e.g., reactor walls). These conditions are met in CVD reactions that liberate CO from metal carbonyls and often employ  $\text{H}_2$  as a reducing agent. In situ formation of Fe and Ni carbonyls could become a source of downstream Fe and Ni contamination for metal carbonyl-based CVD routes. In contrast to the inorganic<sup>42</sup> metal sources in use today, metal–organic precursors are expected to offer greater flexibility and a higher degree of controllability for processing in conventional CVD reactor hardware.

In this article we report a new metal–organic chemical vapor deposition (MOCVD) process that addresses some of the challenges encountered in state-of-the-art vapor-phase TMD growth. We present a new MOCVD process that uses metal–organic and organosulfur precursors and produces wafer-scale 2H- $\text{MoS}_2$  films at short deposition times from tens of seconds to several minutes. We use a pulsed injection strategy to discretize the growth process, which, to our knowledge, is the first reported pulsed MOCVD process for 2D TMD growth.

The relatively low growth temperature of 591 °C employed in this work makes our process thermally compatible with a variety of substrates, including flexible glasses used in consumer electronics.<sup>43</sup> Through extensive postdeposition characterization, we relate film properties to process conditions. We show that few-layer  $\text{MoS}_2$  can be readily produced on 50 mm diameter substrates, with submonolayer control over aggregate film thickness. Chemical analyses show impurity incorporation and ligand removal steps, which suggests that precursor chemistry impacts the film deposition process and that exploration of additional metal–organic precursors may provide new vapor-phase synthetic routes for TMD growth.

## 2. EXPERIMENTAL METHODS

**2.1. Surface Preparation.** Surfaces used for growth characterization consisted of 90 nm thermal  $\text{SiO}_2$  on  $\text{Si}(100)$ . For each growth run, 32 mm × 32 mm coupons were cleaved from a 300 mm wafer, degreased with acetone and methanol, and subsequently dried with a stream of nitrogen. X-ray photoelectron spectra from as-cleaned substrates showed only Si, O, and C species, the latter being ascribed to adventitious carbon.

**2.2. Metal–Organic Chemical Vapor Deposition Growth.** Films were grown in a single-wafer perpendicular flow reactor described elsewhere.<sup>44</sup> Briefly, the reactor consisted of a resistively heated thin-walled stainless steel pedestal, independently heated aluminum walls, and O-ring sealed flanges. Gas flow direction was normal to the plane of the receiving substrate. Walls were maintained at 160 °C and upstream lines were heated to prevent precursor condensation. Substrates were placed on the steel pedestal and heated to a surface temperature of approximately  $591 \pm 1$  °C, measured with a type-K thin-wire thermocouple embedded on a test wafer. Substrates were allowed to thermally equilibrate for 10 min once the heater set point was reached. Reactions were run at 160 Pa with 400 mL/min (standard cubic centimeters per minute, sccm) argon (99.999%) at standard temperature and pressure (STP) with the carrier gas distributed among four delivery lines. Here, STP is defined as 0 °C and 101.33 kPa. The reactor was pumped by a twin-screw pump with an ultimate pressure of approximately 0.01 Pa. The metal precursor was electronic-grade bis(*tert*-butylimido)bis(dimethylamido)-molybdenum,  $(\text{N}^t\text{Bu})_2(\text{NMe})_2\text{Mo}$ , installed in a 300 mL stainless steel ampule, heated to 28 °C in an oven, and delivered by flowing 25 sccm carrier gas over the ampule head space (vapor draw). Electronic-grade diethyl disulfide ( $\text{Et}_2\text{S}_2$ , >98%) was used as the sulfur source and was delivered out of a 100 mL single-port ampule heated to 60 °C. Carrier flow rate in the  $\text{Et}_2\text{S}_2$  line was 100 sccm, with two auxiliary

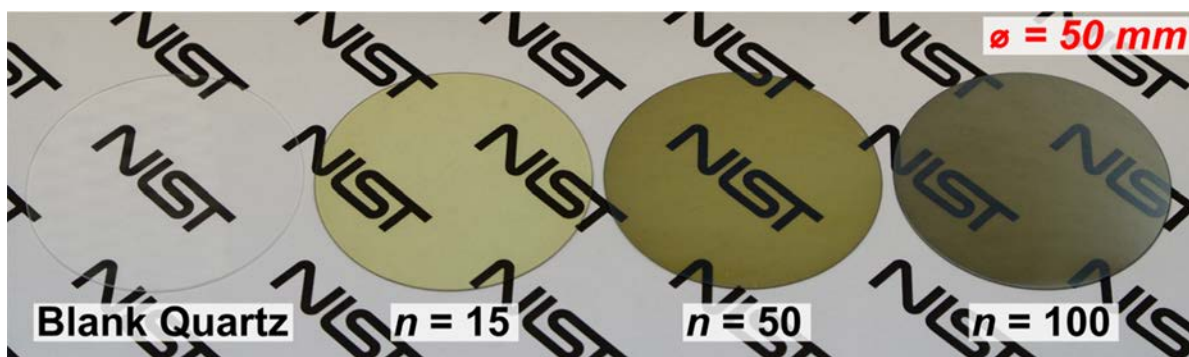


**Figure 2.** Photographs of 50 mm diameter fused quartz wafers demonstrate wafer-scale growth of  $\text{MoS}_2$ . Left to right: a blank wafer and wafers with  $\text{MoS}_2$  deposited with varying numbers of pulses. Logo that appears in the background is used with permission of the National Institute of Standards and Technology (NIST).

lines delivering the balance. In order to limit the amount of  $\text{Et}_2\text{S}_2$  delivered, a 250  $\mu\text{m}$  diameter steel orifice was installed between the ampule and the injection valve. After deposition, the wafer heater was allowed to cool to  $\sim 160$   $^\circ\text{C}$ , at which point the reactor was backfilled with Ar and the wafer was immediately removed and placed on a cold surface. As a result of this procedure, all deposited films were briefly exposed to laboratory ambient conditions at  $\sim 160$   $^\circ\text{C}$  upon removal from the reactor.

Each reaction cycle consisted of 1.5 s coinjections of  $(\text{N}^i\text{Bu})_2(\text{NMe}_2)_2\text{Mo}$  centered on 2.0 s injections of  $\text{Et}_2\text{S}_2$ . Pulse duration for the  $\text{Et}_2\text{S}_2$  was kept slightly longer than the Mo source in order to preclude reactions of  $(\text{N}^i\text{Bu})_2(\text{NMe}_2)_2\text{Mo}$  in the absence of sulfur. After each coinjection of Mo and S reagents, the reactor was purged with 400 sccm Ar for 4.0 s, resulting in a 6.0 s cycle time. A graphical representation of the reaction chamber and the pulse valve timing scheme are shown in Figure 1. High-precision pulse timing and repeatability was incorporated into the injection system by use of low-jitter digital delay generators. In this fashion, reaction cycles were iterated  $n$  times to vary the thicknesses of  $\text{MoS}_2$  deposited. For example, we will write  $n = 15$  to denote 15 injections of  $[(\text{N}^i\text{Bu})_2(\text{NMe}_2)_2\text{Mo} + \text{Et}_2\text{S}_2]$ . By employing pulsed injections, we effectively regulated the amount of material delivered to the growth surface and arbitrarily discretized the time coordinate of the growth process.

**2.3. Characterization.** Raman and photoluminescence (PL) spectra were obtained with 532 nm excitation in a backscattering configuration on a custom-built Raman microprobe system. The incident laser was spatially filtered and sent into the microscope after passing through a linear polarizer to define the excitation polarization. Radiation was introduced into the microscope optical path by use of an angled dielectric edge filter in an injection–rejection configuration. A  $40 \times 0.75$  numerical aperture infinity-corrected microscope objective was used for focusing incident radiation and collecting scattered/emitted radiation. Power levels at the sample were less than about 1 mW for Raman and 0.1 mW for PL spectroscopy. Collected scattered/emitted radiation was coupled to a multimode optical fiber and delivered to a 0.5 m (Raman) and 0.3 m (PL) focal length imaging single spectrograph. Light was detected with a back-illuminated charge-coupled device (CCD) camera system operating at  $-70$   $^\circ\text{C}$  for Raman and  $-75$   $^\circ\text{C}$  for PL. The instrumental bandpass full width at half-maximum (fwhm) was approximately 2.2  $\text{cm}^{-1}$  at 347  $\text{cm}^{-1}$  for Raman and 18.3  $\text{cm}^{-1}$  at 1700  $\text{cm}^{-1}$  for PL spectroscopy. Laser wavelength was determined with a commercial wavemeter.

Cross sectioning for high-resolution transmission electron microscopy (HRTEM) was performed on an FEI Nova Nanolab instrument (FEI Co., Hillsboro, OR). To protect sample integrity, thin layers of C (10 nm) and Pt (250 nm) were deposited by use of an electron beam operating at 5 keV. The final Pt cap was deposited with the ion beam operating at 30 keV. Samples were extracted and thinned by standard lift-out techniques. HRTEM was performed on an FEI Titan 80–300 analytical electron microscope (FEI Co., Hillsboro, OR). Images were

obtained with a multiscan CCD camera with a single  $1024 \times 1024$  pixel detector using 300 keV electrons through a 60  $\mu\text{m}$  aperture at 1 nA of current for 1 s acquisition times. Sample thickness was nominally 100 nm or less for all images obtained. Fourier transformations were calculated by use of Gatan DigitalMicrograph (v3.10) (Gatan Inc., Pleasanton, CA).

X-ray photoelectron spectroscopy (XPS) was carried out on a Kratos Axis Ultra DLD instrument from Kratos Analytical (Chestnut Ridge, NY), which incorporated a monochromated Al  $K\alpha$  source operated at 104 W (8 mA; 13 kV) and a hemispherical analyzer. Spectra were acquired at an analyzer pass energy of 40 eV, and the analysis area was approximately 1 mm by 0.5 mm. Spectra were charge-calibrated against S  $2p_{3/2}$  (S–Mo, 162.0 eV) assigned to  $\text{MoS}_2$ .<sup>45</sup> A low-energy electron gun was used for charge neutralization. Elemental percentages were calculated by taking the average of at least three nonoverlapping measurements, with the uncertainty given as  $\pm 1$  standard deviation of the mean. Film thickness was estimated on the basis of inelastic scattering of Si 2p photoelectrons by an  $\text{MoS}_2$  overlayer. The inelastic mean free path (IMFP) for Si 2p at a kinetic energy of 1383 eV was estimated to be 2.537 nm by use of the TPP-2 M formula as implemented in the NIST Electron Inelastic-Mean-Free-Path Database.<sup>46</sup> Parameters used for the IMFP calculation were  $\rho_{\text{MoS}_2} = 5.06 \text{ g}\cdot\text{cm}^{-3}$  (for bulk molybdenite),<sup>47</sup>  $E_{g,\text{MoS}_2} = 1.8 \text{ eV}$  (monolayer),<sup>2</sup> and 18 valence electrons, where  $\rho$  is the mass density and  $E_g$  is the band gap. Peak fitting was done with the CasaXPS software package (v2.3.17) (Teignmouth, U.K.). Sputter depth profiling was done with 4 keV  $\text{Ar}^+$  ions delivered to the surface at a  $70^\circ$  angle of incidence. The ion beam was rastered over an area of 3 mm  $\times$  3 mm at a current density of approximately 0.5 mA/cm<sup>2</sup>. The analysis area was within the plateau of the sputter crater.

X-ray diffraction (XRD) data were collected on a conventional powder diffractometer by Phillips in the  $\theta$ – $2\theta$  configuration by use of Cu  $K\alpha$  radiation ( $\lambda = 0.15418 \text{ nm}$ ). The XRD scans were analyzed with the MDI-JADE 6.5 software package (Jade 6.5, Materials Data, Inc., Livermore, CA, 2015).  $\text{MoS}_2$   $c$ -lattice parameter was calculated by cell refinement. Complementary two-dimensional X-ray diffraction (XRD<sup>2</sup>) patterns were collected on a Bruker-AXS D8 Discover diffractometer (Bruker Corp., Billerica, MA), equipped with an area detector (Hi-star), using Cu  $K\alpha$  radiation. Intensity of the 0002 reflection from the XRD<sup>2</sup> pattern was angle-integrated along the  $\chi$  direction, which is equivalent to sample tilting in a conventional diffractometer, to produce a “rocking curve”-like plot (see inset in Figure 6) to assess the degree of texture in the film. The angle integrated patterns were examined by use of Bruker AXS Diffracplus EVA software.

Atomic force microscopic (AFM) topographic images were collected on an Asylum Research MFP-3D instrument (Asylum Research, Goleta, CA). The measurements were done in tapping mode with a stiff cantilever (Si, 42 N/m) and a large driving amplitude and set point. Surface roughness values are calculated as the root mean square (rms) of the height data.

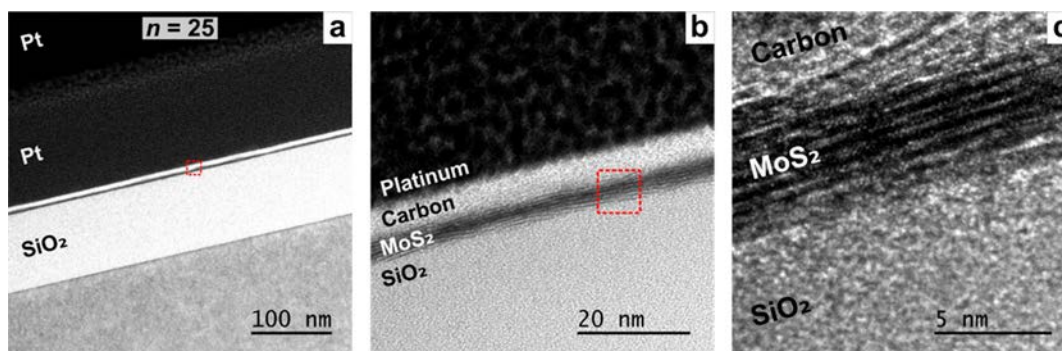


**Figure 3.** HRTEM cross sections from MOCVD-grown MoS<sub>2</sub> on SiO<sub>2</sub>/Si, shown at (a) low, (b) medium, and (c) high magnification.

Scanning electron microscopic (SEM) characterization was done with Hitachi S-4700 (Hitachi High-Technologies Europe GmbH, Krefeld, Germany) and JEOL JSM-7100 (JEOL Ltd., Tokyo, Japan) field-emission instruments operated at 20 kV accelerating voltage with the sample stage tilted to 70° in order to assess the film's morphology.

### 3. RESULTS AND DISCUSSION

Films were grown on wafer substrates via pulsed injections of (N<sup>t</sup>Bu)<sub>2</sub>(NMe<sub>2</sub>)<sub>2</sub>Mo and Et<sub>2</sub>S<sub>2</sub> as described under [Experimental Methods](#). We varied the number of pulses to scale the thickness of the MoS<sub>2</sub> films deposited. The flow distribution in this reactor geometry has been previously modeled<sup>44</sup> by computational fluid dynamics and results in visually uniform coatings on large-area substrates. To demonstrate uniform and large-area deposition of MoS<sub>2</sub>, we grew films of various thicknesses on 50 mm diameter fused quartz wafers. Photographs of wafers with  $n = 0, 15, 50,$  and  $100$  injections of (N<sup>t</sup>Bu)<sub>2</sub>(NMe<sub>2</sub>)<sub>2</sub>Mo and Et<sub>2</sub>S<sub>2</sub> are shown in [Figure 2](#). The coatings are uniform to the eye over the diameter of the wafers and show decreasing optical transmission with increasing film thickness.

Few-layer MoS<sub>2</sub> films were grown and subsequently characterized by cross-sectional HRTEM, Raman spectroscopy, PL spectroscopy, XRD, and XPS. We found that growth on thermal SiO<sub>2</sub> exhibited gross inhomogeneities at  $n < 10$ , associated with nucleation or incomplete surface coverage. In order to characterize the properties of coalesced and continuous films, we focused our attention on films grown with 25 pulses. Cross-sectional HRTEM images from a film deposited with  $n = 25$  are shown in [Figure 3](#). In [Figure 3a](#), MoS<sub>2</sub> can be identified by the dark contrast between the SiO<sub>2</sub> layer and the protective carbon coating. The film is continuous within the field of view, with some areas showing nonuniformities in thickness. Regions of the film that appear to be out of focus may be a result of sample preparation. These regions could be the topmost MoS<sub>2</sub> sheet that has come loose during cross sectioning and is projecting away from the plane of the image. The higher magnification image in [Figure 3b](#) is from the dashed area in [Figure 3a](#). Here, a layered structure is clearly discernible, with some layers exhibiting nonplanar stacking. A higher magnification view in [Figure 3c](#) shows approximately 6 layers present with a total thickness of  $4.08 \pm 0.20$  nm, taken as the average of 10 line measurements in [Figure 3b](#). Interplane spacing was measured to be  $0.68 \pm 0.05$  nm, in agreement with the expected separation between stacked MoS<sub>2</sub> layers.<sup>48</sup>

The orientation of the first few MoS<sub>2</sub> layers with respect to the amorphous substrate may give some insights into the initial nucleation mechanism. Several layers in [Figure 3b](#) emerge from the substrate and terminate back at the substrate a short

distance away, ca. 10 nm. Second, third, and subsequent MoS<sub>2</sub> planes show significantly longer continuity, with some layers extending beyond 50 nm without interruption. Also in [Figure 3b](#), some regions of the image show branching and merging MoS<sub>2</sub> planes. One growth model that would account for these observations is island nucleation. In this model, the anchor points at which the MoS<sub>2</sub> originates out of the substrate could be the initial nucleation sites. Surface-limited reaction of (N<sup>t</sup>Bu)<sub>2</sub>(NMe<sub>2</sub>)<sub>2</sub>Mo with hydroxyl groups was reported for ALD of MoO<sub>3</sub><sup>49</sup> and MoN<sup>50,51</sup> at  $< 325$  °C. If a similar interaction with surface hydroxyls is assumed, the initial formation of Si–O–Mo bonds may also play a role in MoS<sub>2</sub> nucleation. Accordingly, formation of the first MoS<sub>2</sub> layer may be influenced by the substrate chemistry, whereas subsequent layers could form on the basis of interactions with existing MoS<sub>2</sub> surfaces. Differences in layer continuity between the first and subsequent MoS<sub>2</sub> layers give some validity to this distinction. Since the reaction temperatures in this study are low ( $< 600$  °C) relative to furnace-grown TMDs, the Mo adatoms are expected to have limited surface mobility, and therefore, rearrangements at the MoS<sub>2</sub>/SiO<sub>2</sub> interface are less likely. Under such conditions, grain size could be dependent on the initial nucleation process. The interface shown in [Figure 3b,c](#) is remarkably similar to that produced by pulsed laser deposition (PLD)<sup>52</sup> at 700 °C, showing that surface rearrangement may not be favorable even at higher substrate temperatures for fast deposition processes. While we focused this work on wafer-scale growth and pulse-modulated thickness control, deposition at a higher reaction temperature and on crystalline substrates is expected to promote better long-range ordering of MoS<sub>2</sub> basal planes. Further discussion of growth temperature is provided in [Figure S1](#) (Supporting Information).

In addition to comparatively low deposition temperatures afforded by this MOCVD chemistry, controlled and reproducible growth of TMDs is also highly desirable. By employing pulsed injections of precursor, we can impose digital control over film thickness, which is otherwise difficult to achieve with a continuous deposition process. Although a continuous process could have been used, we implemented pulsed injections to mitigate transient effects associated with the depletion of precursor vapor in a vapor draw configuration, as employed in this work. To illustrate thickness scaling that is achievable by our pulsed MOCVD scheme, we systematically varied the number of (N<sup>t</sup>Bu)<sub>2</sub>(NMe<sub>2</sub>)<sub>2</sub>Mo and Et<sub>2</sub>S<sub>2</sub> injections at a wafer temperature of 591 °C and studied the resultant films by XPS. By measuring the attenuation of the Si 2p photoelectrons originating in the SiO<sub>2</sub> layer, we were able to estimate the average thickness of the MoS<sub>2</sub> overlayer over the sampled area

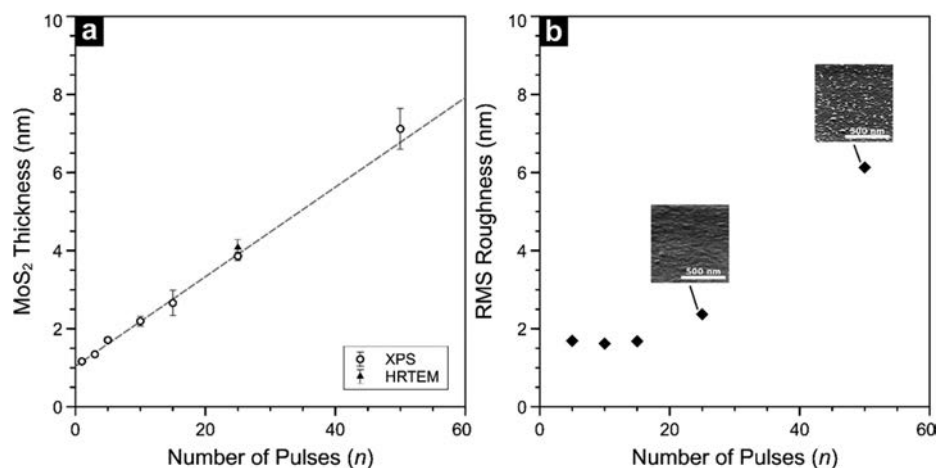


**Figure 4.** (a) Film thickness, estimated from Si 2p photoelectron attenuation, plotted as a function of pulse count. Error bars represent 1 standard deviation of the mean. (b) Root-mean-square surface roughness as determined by AFM. (Insets) Perspective view ( $70^\circ$  tilt) SEM images for 25 and 50 pulses.

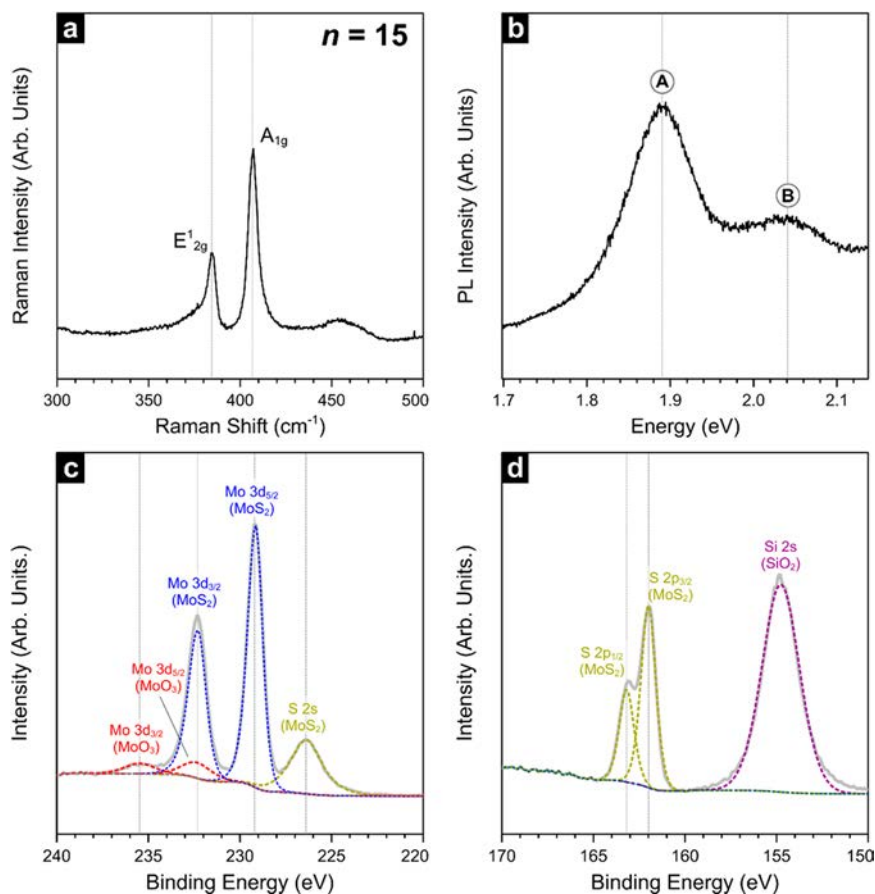


**Figure 5.** (a) Raman and (b) PL spectra for a few-layer MOCVD  $\text{MoS}_2$  film ( $n = 15$ ) deposited on  $\text{SiO}_2$ . X-ray photoelectron spectra from the same surfaces are shown for (c) Mo 3d and (d) S 2p regions.

(see Supporting Information for details). Given the large analysis area of XPS ( $\sim 0.5 \text{ mm}^2$ ) compared to the  $\text{MoS}_2$  crystallite size, film thicknesses calculated from XPS are representative of the amount of material on the surface without accounting for growth mode. Figure 4a shows the results of this analysis. We found that film thickness increases linearly with  $n$ , and the MOCVD process gives rise to Mo 3d signal after a single injection of the reactants (Figure S2). Since the reactivity of  $(\text{N}^t\text{Bu})_2(\text{NMe}_2)_2\text{Mo}$  with hydroxylated surfaces is known,

the lack of a chemisorption delay is not surprising. Interestingly, the thickness intercept in Figure 4a is nonzero, which could indicate the presence of an interfacial layer that develops during nucleation or a surface contamination layer that exists prior to deposition. These would be reasonable possibilities since the substrates do not undergo in situ cleaning before growth. While the origin of this offset is not clear, the linear trend in Figure 4a demonstrates the level of thickness control afforded by the pulsed injection strategy. The aggregate growth rate is

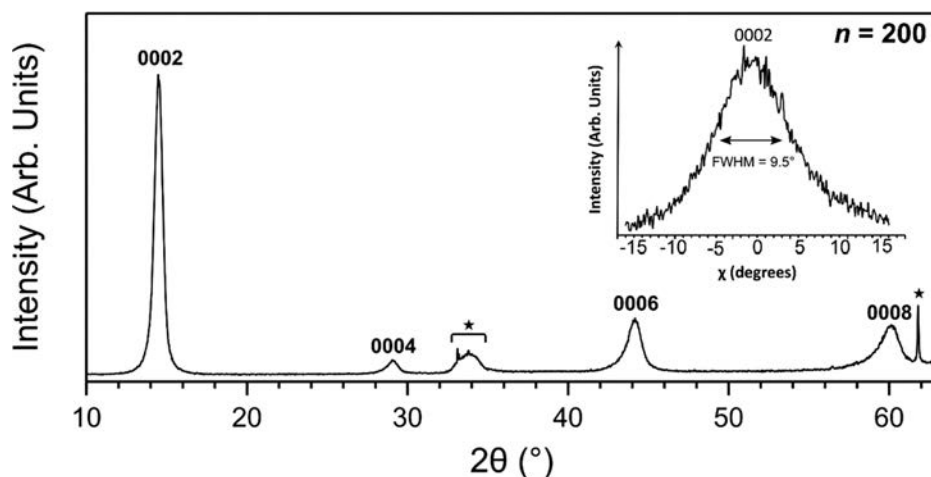


**Figure 6.**  $\theta$ - $2\theta$  XRD scans from thick MoS<sub>2</sub> films ( $\sim 25$  nm,  $n = 200$ ) grown at 591 °C. Absence of the  $hkl$  reflections other than from the {0002} family is evidence for 0002 texture in the film. A high degree of texture is also evident from a relatively narrow rocking curve shown in the inset, which shows an integrated intensity for the 0002 reflection vs  $\chi$ -angle produced from XRD<sup>2</sup> diffraction (not shown). Reflections identified with a star (★) on the  $\theta$ - $2\theta$  scan are from the Si(100) substrate. The lattice parameter is calculated as  $c = 1.2306(5)$  nm.

determined to be 0.12 nm/pulse, which is equivalent to <1 monolayer (ML) of MoS<sub>2</sub> deposited per injection, when considered on a planar basis. Given that 2H-MoS<sub>2</sub> is a layered crystal with fixed  $d$  spacing, an aggregate growth rate less than  $d$  suggests that surface coverage is less than unity per pulse. The aggregate thickness control achieved by our MOCVD approach demonstrates that a pulsed metering of the precursor delivered to the substrate can provide fine control over film thickness for a fast TMD deposition process. For further analysis of the way in which growth proceeds, we turn to AFM.

Figure 4b shows the evolution of surface roughness for the same range of thicknesses analyzed by XPS. For  $n \leq 15$ , film roughness remains below 2 nm. Within this regime, films are relatively smooth and exhibit a uniform distribution of small features <20 nm in lateral dimensions, as shown in Figure S3. At  $n = 25$ , roughness increases to 2.4 nm, and it continues to rise, reaching 6 nm at  $n = 50$ . Despite the large roughness factor, all MoS<sub>2</sub> on the surface is accounted for by XPS since Si 2p photoelectrons have a finite escape probability through an MoS<sub>2</sub> layer up to  $\sim 8$  nm thick. Contrasting the linear growth rate measured by XPS to the onset of surface roughening at  $n = 25$ , we postulate that three-dimensional (3D) or out-of-plane MoS<sub>2</sub> growth takes place beyond  $\sim 4$  nm of growth. Indeed, we find that, beyond 50 pulses, films continue to roughen. Accompanying SEM images show that the rough areas evident at  $n = 25$  take the form of randomly oriented features by  $n = 50$  and eventually grow into sharp platelets emerging from the surface at  $n = 100$  (Figure S4). Additional deposition ( $n = 200$ ) produces a continuous surface with rounded features. One potential explanation for this evolution in film morphology is a growth process with a distinct nucleation phase. At  $n \leq 15$ , the growth could be dominated by precursor-substrate interactions, as the initial few monolayers of MoS<sub>2</sub> are formed. Subsequent deposition of MoS<sub>2</sub> on existing MoS<sub>2</sub> sites includes a 3D growth component, where out-of-plane crystallites can form alongside the layered structure, confirmed by TEM and diffraction measurements (as will be discussed).

The complex evolution of MoS<sub>2</sub> layering, surface coverage, and morphology is a confounding factor for spectroscopic measurements. For this reason we will limit spectroscopic analyses to few-layer MoS<sub>2</sub> to confirm optical and optoelec-

tronic characteristics. We found that PL yield for our MoS<sub>2</sub> films was maximized around  $n = 15$ ; therefore, we focused subsequent analysis on few-layer material produced with 15 pulses. The Raman spectrum in Figure 5a exhibits in-plane ( $E_{2g}^1$ ) and out-of-plane ( $A_{1g}$ ) modes associated with 2H-MoS<sub>2</sub> at 384.7 and 407.2 cm<sup>-1</sup>, respectively. The broad asymmetric feature at 454 cm<sup>-1</sup> has been ascribed to a superposition of second-order zone-edge phonon 2LA(M) and first-order optical phonon  $A_{2u}$ .<sup>53</sup> These modes were previously observed in bilayer MoS<sub>2</sub> from natural crystals. While the position and separation of  $E_{2g}^1$  and  $A_{1g}$  are often correlated with the number of MoS<sub>2</sub> layers,<sup>53,54</sup> quantitative relationships have been established only for exfoliated single-crystal materials. Since line positions are influenced by the local electronic environment, an exact determination of film thickness for CVD films is complicated by factors such as local inhomogeneities (e.g., simultaneous sampling of multiple grains), rotational stacking faults, and grain size.<sup>55</sup> For these reasons, we rely on XPS and HRTEM for thickness measurements as described previously.

To further assess the optoelectronic properties of our MOCVD films, we turn to photoluminescence (PL) spectroscopy. PL can often complement Raman spectroscopy, since large differences in PL yield can help discriminate between monolayer and few-layer MoS<sub>2</sub>.<sup>2</sup> The PL spectrum of the same surface from Figure 5a is shown in Figure 5b. The two broad features centered at 2.04 eV (656.0 nm) and 1.89 eV (607.6 nm) are assigned to the A and B excitons, respectively, originating from the direct gap transition at the K point. The energy of the A and B excitons is consistent with measurements from natural MoS<sub>2</sub> samples, and the simultaneous presence of the two transitions generally suggests a multilayer film.<sup>2,56,57</sup> As with Raman, existing literature on PL of MoS<sub>2</sub> focuses on single-crystal measurements. Since our MOCVD films are polycrystalline and likely comprise an ensemble of layers (i.e., a mixture of different layer numbers), a reliable determination of thickness or layer number is left to other measurements.

Chemical analysis by XPS of the same films produced with  $n = 15$  is shown in Figure 5c,d. The high-resolution spectrum in Figure 5c shows Mo 3d and S 2s core levels. Two types of Mo species are apparent due to the presence of two Mo 3d doublets. The lower binding energy (BE) doublet is ascribed to

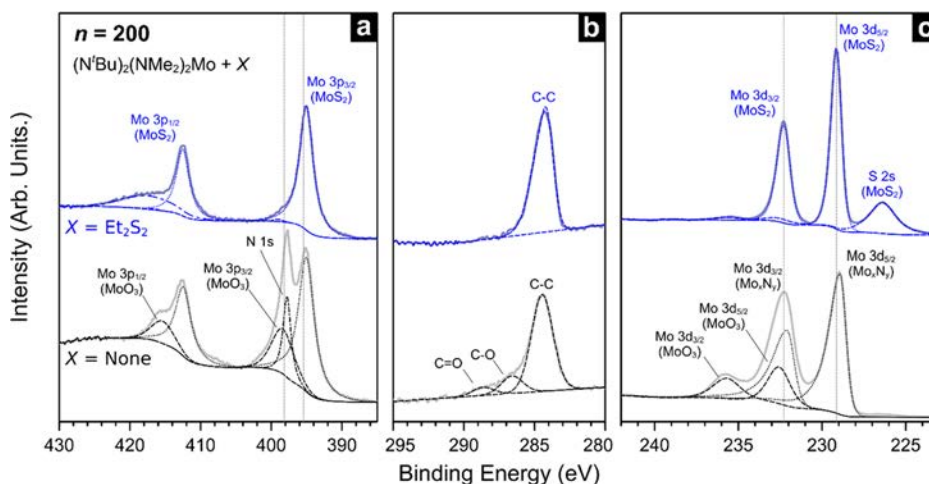


**Figure 7.** High-resolution XPS spectra and synthetic peak fitting in (a) Mo 3p, (b) C 1s, and (c) Mo 3d core levels from films prepared with  $n = 200$  pulses, with ( $X = \text{Et}_2\text{S}_2$ ) and without ( $X = \text{none}$ ) a sulfur coreactant.

$\text{MoS}_2$ , with the  $3d_{5/2}$  and  $3d_{3/2}$  spin-orbit components positioned at 229.1 and 232.3 eV ( $\Delta = 3.15$  eV), respectively, comparable to values reported for natural  $\text{MoS}_2$  crystals.<sup>45</sup> Oxidized Mo is observed as a higher BE doublet at 232.3 and 235.5 eV, likely from the oxidation of unsaturated Mo sites upon exposure to air. This thin oxide layer is typically described as  $\text{MoO}_3$  and is known to develop<sup>58</sup> over time on both natural and synthetic  $\text{MoS}_2$ . A broad S 2s transition is found at 226.4 eV, as expected for  $\text{MoS}_2$ . For the corresponding S 2p transition in Figure 5d, only one species of S is apparent, with the position of the S 2p doublet (162.2 and 163.3 eV) consistent with S–Mo bonding in  $\text{MoS}_2$ . The presence of the Si 2s peak at 154.8 eV confirms that the  $\text{MoS}_2$  film is thin enough to transmit photoelectrons from the underlying  $\text{SiO}_2/\text{Si}$  substrate (<8 nm). The main impurity found in the films is graphitic carbon, which will be discussed in more detail.

To investigate the crystal structure of the MOCVD films, we grew  $\sim 25$  nm thick  $\text{MoS}_2$  with 200 pulses of Mo and S precursors and analyzed the XRD patterns generated therefrom. The XRD pattern in Figure 6 was obtained by measuring a  $\theta$ – $2\theta$  scan from such a film. The as-grown film is crystallized into the single-phase 2H- $\text{MoS}_2$  hexagonal polytype with space group  $P6_3/mmc$  ( $D_{6h}^4$  in Schönflies notation, or #194 in ITC).<sup>59</sup> In agreement with the layered structure apparent in the HRTEM images, strong (000 $l$ ) texturing in the  $2\theta$  scan indicates  $c$ -plane-oriented growth. Refined lattice parameter  $c = 1.2306(5)$  nm was obtained by use of powder diffraction file 01-073-1508 (ICCD, 2010) and is consistent with values reported in the literature.<sup>60,61</sup> Plane spacing of  $d = c/2 = 0.612$  nm was also in excellent agreement with values reported elsewhere.<sup>62</sup> Since the XRD patterns were obtained from thick  $\text{MoS}_2$  specimens ( $n = 200$ ,  $\sim 25$  nm), reasonable agreement between the calculated  $d$  and HRTEM layer spacing for few-layer  $\text{MoS}_2$  ( $n = 25$ ) indicates that a considerable degree of crystallinity persists even for thick  $\text{MoS}_2$  films. The relatively narrow rocking curve shown in the inset to Figure 6 is further evidence to the high level of texturing in the MOCVD films.

To assess the bulk composition and stoichiometry of our MOCVD-grown material, we used the same  $\sim 25$  nm thick  $\text{MoS}_2$  film ( $n = 200$ ) for XPS analysis. The main impurity in the film was found to be carbon, which is discussed in more detail. We found that C accumulation in the film was correlated with the number of pulses used to grow the film. To exclude

contributions from adventitious hydrocarbons, we sputtered the  $\text{MoS}_2$  surface prior to compositional analysis. The depth profile obtained from this analysis is shown in Supporting Information (Figure S5). Elemental impurities left in the film after 60 s of  $\text{Ar}^+$  sputtering were carbon (5%) and oxygen (5%). The true internal composition of the film could not be measured by XPS, as longer ion milling suffers from preferential sputtering of sulfur.<sup>63</sup> Film stoichiometry near the surface was determined to be S:Mo =  $1.95 \pm 0.01$  as calculated from the Mo 3d and S 2p core levels. A small degree of sulfur deficiency due to undercoordinated Mo edge sites has also been noted for other synthetic  $\text{MoS}_2$  films and is likewise encountered in natural single crystals.<sup>64</sup>

In addition to process characteristics and optoelectronic properties, we also evaluated the growth chemistry of our MOCVD process. To assess the role of each precursor in the deposition process, we grew thick films at 591 °C with and without a sulfur source and compared the binding state of Mo, N, C, and S core electrons. Photoelectron spectra from these films are shown in Figure 7, where the lower spectra (black) represent films grown from  $(\text{N}^t\text{Bu})_2(\text{NMe}_2)_2\text{Mo}$  alone and the upper spectra (blue) denote those grown from the Mo source together with  $\text{Et}_2\text{S}_2$ . The Mo 3p region for the surface exposed to sulfur, in Figure 7a, shows evidence for a single Mo species that dominates the spectrum. Here, the doublet at 395.0 and 412.5 eV satisfies the 2:1 area ratio for spin-orbit splitting and is ascribed to  $\text{MoS}_2$ . The broad feature at 417.4 eV is likely a surface plasmon peak, also observed in pristine  $\text{MoS}_2$  specimens.<sup>45</sup> While a small  $\text{MoO}_3$  component can be discerned in the spectrum, this contribution is more readily evident in the Mo 3d region. In the spectrum from a surface exposed to the Mo precursor only (lower trace), two doublets are clearly resolved. However, the doublets alone do not fully account for the Mo 3p core spectrum, since the relative intensity relationship between the  $3p_{3/2}$  and  $3p_{1/2}$  peaks requires the presence of an additional component at 397.8 eV. This peak corresponds to the N 1s transition, likely a result of N–Mo bonding. The presence of the N KLL Auger transition in the survey spectrum further corroborates this hypothesis (Figure S6). The position of the lower BE Mo  $3p_{3/2}$  component is consistent with either a sulfide or a nitride species. We discount the possibility of metallic Mo, since  $\text{Mo}^0$  would be expected at a lower binding energy. Indeed, the Mo 3d and S 2s regions in

Figure 7c clearly indicate the presence of MoS<sub>2</sub> when Et<sub>2</sub>S<sub>2</sub> is used in the reaction and show oxidized Mo in addition to the lower BE doublet when the reaction is run without Et<sub>2</sub>S<sub>2</sub>. The relatively large contribution from MoO<sub>3</sub> in the Mo-only film indicates that a significant fraction of the deposited film consists of unsaturated Mo (possibly metallic) that is subsequently oxidized upon removal from the reactor (~160 °C). The position of the lower BE Mo 3d doublet is consistent with either MoS<sub>2</sub> or Mo<sub>x</sub>N<sub>y</sub>, but the relative absence of sulfur (<3%, from residual sulfur in the reactor) and the detection of N 1s favors the latter possibility. The peak shape of the Mo 3d<sub>5/2</sub> transition at 228.9 eV is also consistent with molybdenum nitride, which is known to produce asymmetric peak shapes since MoN is a good electrical conductor.<sup>65</sup>

The interpretation of the Mo regions is corroborated by the C 1s spectra, shown in Figure 7b. For the films grown with and without a sulfur source, the salient difference in the C 1s region is the absence or presence of oxidized carbon species. For the surface exposed to Et<sub>2</sub>S<sub>2</sub>, the C 1s region shows a single asymmetric peak at 284.2 eV, which is ascribed to graphitic carbon due to its unique asymmetric peak shape.<sup>66</sup> In contrast, the surface that was exposed only to the Mo precursor produces a C 1s spectrum with two additional peaks at 286.6 and 288.6 eV. The former peak most likely stems from C–O bonding, with the latter peak position being high enough in BE to denote C=O or C–N. Since the Mo and S precursors do not possess any oxygen-containing functionality, the incorporation of O into the films is largely a result of atmospheric exposure, although a low background of oxygen in the reactor cannot be excluded. The notable absence of distinct C–O or C=O related peaks for the Et<sub>2</sub>S<sub>2</sub>-exposed surface makes it unlikely that adventitious carbon is the source of these oxygen-containing groups. A plausible explanation of the spectra is the generation of C–O and C=O functionalities on the film surface upon exposure to air, possibly by oxidation of unreacted ligands on the surface. This suggests that a ligand removal mechanism may play a part in the deposition process and Et<sub>2</sub>S<sub>2</sub> is not simply a source of sulfur atoms but rather a reactant that interacts with the growth surface or the metal precursor in the thermal boundary layer. This hypothesis is further supported by the observation that residual nitrogen remains in the films when the sulfur source is omitted, but N-containing ligands (amides and imides) are absent when Et<sub>2</sub>S<sub>2</sub> is used during growth. Therefore, the chemistry behind our MOCVD MoS<sub>2</sub> growth is not a simple case of Mo<sup>0</sup> deposition followed by sulfurization. This apparent interaction between precursor ligands is also distinct from processes that use Mo(CO)<sub>6</sub>, which thermally decomposes<sup>67</sup> into Mo<sup>0</sup> and can be subsequently sulfurized.<sup>68</sup> Since reaction chemistry plays a part in growth, our MOCVD process highlights the opportunities in new precursor design and reaction schemes for scalable and controllable TMD growth processes.

#### 4. CONCLUSION

Large-area and controllable growth of TMDs requires reaction chemistries that are compatible with industrially relevant growth techniques such as MOCVD. We have presented process characteristics and film properties for wafer-scale growth of 2H-MoS<sub>2</sub> using metal–organic and organosulfur reagents in a pulsed MOCVD reactor. Polycrystalline few-layer films were produced at comparatively low temperatures (<600 °C) with fast deposition times on the order of seconds to minutes. Pulsed injections of precursor vapors facilitated

excellent control over film thickness, producing films of <1–25 nm in thickness, with a growth rate of 0.12 nm/pulse. Our process demonstrates the feasibility of using low vapor pressure metal–organic sources as reagents for TMD growth and presents a viable alternative to various inorganic sources used up to this point. Moreover, the large library of metal–organic compounds offers process designers the flexibility to choose reagents on the basis of volatility, thermal stability, and reactivity. While the temperature of our process imposes limitations on TMD grain size, low temperature and fast processing could be advantageous for applications requiring thermal compatibility with flexible glass substrates and low cycle times for roll-to-roll processing.

#### ■ ASSOCIATED CONTENT

##### Supporting Information

The Supporting Information is available free of charge on the ACS Publications website at DOI: 10.1021/acs.chemmater.7b01367.

Additional text, seven figures, and two tables showing dependence of film crystallinity on substrate temperature, AFM and SEM images, XPS spectra of early nucleation, XPS depth profile and survey scans, and thickness uniformity on quartz wafers (PDF)

#### ■ AUTHOR INFORMATION

##### Corresponding Author

\*E-mail [berc.kalanyan@nist.gov](mailto:berc.kalanyan@nist.gov).

##### ORCID

Berc Kalanyan: 0000-0003-3508-9693

Elias Garratt: 0000-0002-0331-3876

##### Notes

The authors declare no competing financial interest.

#### ■ ACKNOWLEDGMENTS

We thank SUNY Poly SEMATECH (formerly SEMATECH) for providing diethyl disulfide (Air Products) and EMD Performance Materials for supplying the (N<sup>t</sup>Bu)<sub>2</sub>(NMe<sub>2</sub>)<sub>2</sub>Mo precursor. Certain commercial equipment, instruments, and materials are identified in this publication to adequately specify the experimental procedure. Such identification in no way implies approval, recommendation, or endorsement by the National Institute of Standards and Technology, nor does it imply that the equipment, instruments, or materials identified are necessarily the best available for the purpose.

#### ■ REFERENCES

- (1) Mak, K. F.; Shan, J. Photonics and Optoelectronics of 2D Semiconductor Transition Metal Dichalcogenides. *Nat. Photonics* **2016**, *10*, 216–226.
- (2) Mak, K. F.; Lee, C.; Hone, J.; Shan, J.; Heinz, T. F. Atomically Thin MoS<sub>2</sub>: A New Direct-Gap Semiconductor. *Phys. Rev. Lett.* **2010**, *105*, No. 136805.
- (3) Radisavljevic, B.; Radenovic, A.; Brivio, J.; Giacometti, V.; Kis, A. Single-Layer MoS<sub>2</sub> Transistors. *Nat. Nanotechnol.* **2011**, *6*, 147–150.
- (4) Kim, S.; Konar, A.; Hwang, W.-S.; Lee, J. H.; Lee, J.; Yang, J.; Jung, C.; Kim, H.; Yoo, J.-B.; Choi, J.-Y.; et al. High-Mobility and Low-Power Thin-Film Transistors Based on Multilayer MoS<sub>2</sub> Crystals. *Nat. Commun.* **2012**, *3*, No. 1011.
- (5) Sarkar, D.; Xie, X.; Liu, W.; Cao, W.; Kang, J.; Gong, Y.; Kraemer, S.; Ajayan, P. M.; Banerjee, K. A Subthermionic Tunnel Field-Effect Transistor with an Atomically Thin Channel. *Nature* **2015**, *526*, 91–95.

- (6) Mak, K. F.; He, K.; Shan, J.; Heinz, T. F. Control of Valley Polarization in Monolayer MoS<sub>2</sub> by Optical Helicity. *Nat. Nanotechnol.* **2012**, *7*, 494–498.
- (7) Cheng, P.; Sun, K.; Hu, Y. H. Memristive Behavior and Ideal Memristor of 1T Phase MoS<sub>2</sub> Nanosheets. *Nano Lett.* **2016**, *16*, 572–576.
- (8) Liu, B.; Chen, L.; Liu, G.; Abbas, A. N.; Fathi, M.; Zhou, C. High-Performance Chemical Sensing Using Schottky-Contacted Chemical Vapor Deposition Grown Monolayer MoS<sub>2</sub> Transistors. *ACS Nano* **2014**, *8*, 5304–5314.
- (9) Roy, K.; Padmanabhan, M.; Goswami, S.; Sai, T. P.; Ramalingam, G.; Raghavan, S.; Ghosh, A. Graphene-MoS<sub>2</sub> Hybrid Structures for Multifunctional Photoresponsive Memory Devices. *Nat. Nanotechnol.* **2013**, *8*, 826–830.
- (10) Ross, J. S.; Klement, P.; Jones, A. M.; Ghimire, N. J.; Yan, J.; Mandrus, D. G.; Taniguchi, T.; Watanabe, K.; Kitamura, K.; Yao, W.; et al. Electrically Tunable Excitonic Light-Emitting Diodes Based on Monolayer WSe<sub>2</sub> P-N Junctions. *Nat. Nanotechnol.* **2014**, *9*, 268–272.
- (11) De Fazio, D.; Goykhman, I.; Yoon, D.; Bruna, M.; Eiden, A.; Milana, S.; Sassi, U.; Barbone, M.; Dumcenco, D.; Marinov, K.; et al. High Responsivity, Large-Area Graphene/MoS<sub>2</sub> Flexible Photodetectors. *ACS Nano* **2016**, *10*, 8252–8262.
- (12) Lopez-Sanchez, O.; Lembke, D.; Kayci, M.; Radenovic, A.; Kis, A. Ultrasensitive Photodetectors Based on Monolayer MoS<sub>2</sub>. *Nat. Nanotechnol.* **2013**, *8*, 497–501.
- (13) Xie, X.; Ao, Z.; Su, D.; Zhang, J.; Wang, G. MoS<sub>2</sub>/Graphene Composite Anodes with Enhanced Performance for Sodium-Ion Batteries: The Role of the Two-Dimensional Heterointerface. *Adv. Funct. Mater.* **2015**, *25*, 1393–1403.
- (14) Smolyanitsky, A.; Jakobson, B. I.; Wassenaar, T. A.; Paulechka, E.; Kroenlein, K. A MoS<sub>2</sub>-Based Capacitive Displacement Sensor for DNA Sequencing. *ACS Nano* **2016**, *10*, 9009–9016.
- (15) Zhu, C.; Zeng, Z.; Li, H.; Li, F.; Fan, C.; Zhang, H. Single-Layer MoS<sub>2</sub>-Based Nanoprobes for Homogeneous Detection of Biomolecules. *J. Am. Chem. Soc.* **2013**, *135*, 5998–6001.
- (16) Wang, F.; Wang, Z.; Xu, K.; Wang, F.; Wang, Q.; Huang, Y.; Yin, L.; He, J. Tunable GaTe-MoS<sub>2</sub> van Der Waals P-n Junctions with Novel Optoelectronic Performance. *Nano Lett.* **2015**, *15*, 7558–7566.
- (17) Lee, G.-H.; Yu, Y.-J.; Cui, X.; Petrone, N.; Lee, C.-H.; Choi, M. S.; Lee, D.-Y.; Lee, C.; Yoo, W. J.; Watanabe, K.; et al. Flexible and Transparent MoS<sub>2</sub> Field-Effect Transistors on Hexagonal Boron Nitride-Graphene Heterostructures. *ACS Nano* **2013**, *7*, 7931–7936.
- (18) Laskar, M. R.; Nath, D. N.; Ma, L.; Lee, E. W.; Il; Lee, C. H.; Kent, T.; Yang, Z.; Mishra, R.; Roldan, M. A.; Idrobo, J.-C.; et al. P-Type Doping of MoS<sub>2</sub> Thin Films Using Nb. *Appl. Phys. Lett.* **2014**, *104*, No. 092104.
- (19) Zhang, K.; Feng, S.; Wang, J.; Azcatl, A.; Lu, N.; Addou, R.; Wang, N.; Zhou, C.; Lerach, J.; Bojan, V.; et al. Manganese Doping of Monolayer MoS<sub>2</sub>: The Substrate Is Critical. *Nano Lett.* **2015**, *15*, 6586–6591.
- (20) Tarasov, A.; Zhang, S.; Tsai, M.-Y.; Campbell, P. M.; Graham, S.; Barlow, S.; Marder, S. R.; Vogel, E. M. Controlled Doping of Large-Area Trilayer MoS<sub>2</sub> with Molecular Reductants and Oxidants. *Adv. Mater.* **2015**, *27*, 1175–1181.
- (21) Gao, J.; Kim, Y. D.; Liang, L.; Idrobo, J. C.; Chow, P.; Tan, J.; Li, B.; Li, L.; Sumpter, B. G.; Lu, T.-M.; et al. Transition-Metal Substitution Doping in Synthetic Atomically Thin Semiconductors. *Adv. Mater.* **2016**, *28*, 9735–9743.
- (22) Komsa, H.-P.; Krasheninnikov, A. V. Two-Dimensional Transition Metal Dichalcogenide Alloys: Stability and Electronic Properties. *J. Phys. Chem. Lett.* **2012**, *3*, 3652–3656.
- (23) Esmaili-Rad, M. R.; Salahuddin, S. High Performance Molybdenum Disulfide Amorphous Silicon Heterojunction Photodetector. *Sci. Rep.* **2013**, *3*, No. 2345.
- (24) Deng, Y.; Luo, Z.; Conrad, N. J.; Liu, H.; Gong, Y.; Najmaei, S.; Ajayan, P. M.; Lou, J.; Xu, X.; Ye, P. D. Black Phosphorus–Monolayer MoS<sub>2</sub> van der Waals Heterojunction P–n Diode. *ACS Nano* **2014**, *8*, 8292–8299.
- (25) Ruzmetov, D.; Zhang, K.; Stan, G.; Kalanyan, B.; Bhimanapati, G. R.; Eichfeld, S. M.; Burke, R. A.; Shah, P. B.; O'Regan, T. P.; Crowne, F. J.; et al. Vertical 2D/3D Semiconductor Heterostructures Based on Epitaxial Molybdenum Disulfide and Gallium Nitride. *ACS Nano* **2016**, *10*, 3580–3588.
- (26) Ubaldini, A.; Jacimovic, J.; Ubrig, N.; Giannini, E. Chloride-Driven Chemical Vapor Transport Method for Crystal Growth of Transition Metal Dichalcogenides. *Cryst. Growth Des.* **2013**, *13*, 4453–4459.
- (27) Hu, T.; Bian, K.; Tai, G.; Zeng, T.; Wang, X.; Huang, X.; Xiong, K.; Zhu, K. Oxidation-Sulfidation Approach for Vertically Growing MoS<sub>2</sub> Nanofilms Catalysts on Molybdenum Foils as Efficient HER Catalysts. *J. Phys. Chem. C* **2016**, *120*, 25843–25850.
- (28) Tai, G.; Zeng, T.; Yu, J.; Zhou, J.; You, Y.; Wang, X.; Wu, H.; Sun, X.; Hu, T.; Guo, W. Fast and Large-Area Growth of Uniform MoS<sub>2</sub> Monolayers on Molybdenum Foils. *Nanoscale* **2016**, *8*, 2234–2241.
- (29) Zhan, Y.; Liu, Z.; Najmaei, S.; Ajayan, P. M.; Lou, J. Large-Area Vapor-Phase Growth and Characterization of MoS<sub>2</sub> Atomic Layers on a SiO<sub>2</sub> Substrate. *Small* **2012**, *8*, 966–971.
- (30) Lee, Y.-H.; Yu, L.; Wang, H.; Fang, W.; Ling, X.; Shi, Y.; Lin, C.-T.; Huang, J.-K.; Chang, M.-T.; Chang, C.-S.; et al. Synthesis and Transfer of Single-Layer Transition Metal Disulfides on Diverse Surfaces. *Nano Lett.* **2013**, *13*, 1852–1857.
- (31) Rong, Y.; Fan, Y.; Koh, A. L.; Robertson, A. W.; He, K.; Wang, S.; Tan, H.; Sinclair, R.; Warner, J. H. Controlling Sulphur Precursor Addition for Large Single Crystal Domains of WS<sub>2</sub>. *Nanoscale* **2014**, *6*, 12096–12103.
- (32) Xia, J.; Huang, X.; Liu, L.-Z.; Wang, M.; Wang, L.; Huang, B.; Zhu, D.-D.; Li, J.-J.; Gu, C.-Z.; Meng, X.-M. CVD Synthesis of Large-Area, Highly Crystalline MoSe<sub>2</sub> Atomic Layers on Diverse Substrates and Application to Photodetectors. *Nanoscale* **2014**, *6*, 8949–8955.
- (33) Zhou, L.; Xu, K.; Zubair, A.; Liao, A. D.; Fang, W.; Ouyang, F.; Lee, Y.-H.; Ueno, K.; Saito, R.; Palacios, T.; et al. Large-Area Synthesis of High-Quality Uniform Few-Layer MoTe<sub>2</sub>. *J. Am. Chem. Soc.* **2015**, *137*, 11892–11895.
- (34) Keyshar, K.; Gong, Y.; Ye, G.; Brunetto, G.; Zhou, W.; Cole, D. P.; Hackenberg, K.; He, Y.; Machado, L.; Kabbani, M.; et al. Chemical Vapor Deposition of Monolayer Rhenium Disulfide (ReS<sub>2</sub>). *Adv. Mater.* **2015**, *27*, 4640–4648.
- (35) Yu, Y.; Li, C.; Liu, Y.; Su, L.; Zhang, Y.; Cao, L. Controlled Scalable Synthesis of Uniform, High-Quality Monolayer and Few-Layer MoS<sub>2</sub> Films. *Sci. Rep.* **2013**, *3*, No. 1866.
- (36) Kang, K.; Xie, S.; Huang, L.; Han, Y.; Huang, P. Y.; Mak, K. F.; Kim, C.-J.; Muller, D.; Park, J. High-Mobility Three-Atom-Thick Semiconducting Films with Wafer-Scale Homogeneity. *Nature* **2015**, *520*, 656–660.
- (37) Tan, L. K.; Liu, B.; Teng, J. H.; Guo, S.; Low, H. Y.; Loh, K. P. Atomic Layer Deposition of a MoS<sub>2</sub> Film. *Nanoscale* **2014**, *6*, 10584–10588.
- (38) Groven, B.; Heyne, M.; Nalin Mehta, A.; Bender, H.; Nuytten, T.; Meersschaut, J.; Conard, T.; Verdonck, P.; Van Elshocht, S.; Vandervorst, W.; et al. Plasma-Enhanced Atomic Layer Deposition of Two-Dimensional WS<sub>2</sub> from WF<sub>6</sub>, H<sub>2</sub> Plasma, and H<sub>2</sub>S. *Chem. Mater.* **2017**, *29*, 2927–2938.
- (39) Eichfeld, S. M.; Hossain, L.; Lin, Y.-C.; Piasecki, A. F.; Kupp, B.; Birdwell, A. G.; Burke, R. A.; Lu, N.; Peng, X.; Li, J.; et al. Highly Scalable, Atomically Thin WSe<sub>2</sub> Grown via Metal–Organic Chemical Vapor Deposition. *ACS Nano* **2015**, *9*, 2080–2087.
- (40) *Chemical Vapor Deposition: Precursors, Processes and Applications*; Jones, A. C., Hitchman, M. L., Eds.; Royal Society of Chemistry: Cambridge, U.K., 2009; DOI: 10.1039/9781847558794.
- (41) Ludlum, K. H.; Eischens, R. P. Carbonyl Formation in Stainless Steel Infrared Cells. *Surf. Sci.* **1973**, *40*, 397–398.
- (42) Salzer, A. Nomenclature of Organometallic Compounds of the Transition Elements (IUPAC Recommendations 1999). *Pure Appl. Chem.* **1999**, *71*, 1557–1585.

- (43) Garner, S.; Glaesemann, S.; Li, X. Ultra-Slim Flexible Glass for Roll-to-Roll Electronic Device Fabrication. *Appl. Phys. A: Mater. Sci. Process.* **2014**, *116*, 403–407.
- (44) Kimes, W. A.; Moore, E. F.; Maslar, J. E. Perpendicular-Flow, Single-Wafer Atomic Layer Deposition Reactor Chamber Design for Use with in Situ Diagnostics. *Rev. Sci. Instrum.* **2012**, *83*, No. 083106.
- (45) Ganta, D.; Sinha, S.; Haasch, R. T. 2-D Material Molybdenum Disulfide Analyzed by XPS. *Surf. Sci. Spectra* **2014**, *21*, 19–27.
- (46) Powell, C. J.; Jablonski, A. *NIST Electron Inelastic-Mean-Free-Path Database*, version 1.2; National Institute of Standards and Technology, Gaithersburg, MD, 2010; <https://www.nist.gov/srd/nist-standard-reference-database-71>.
- (47) Haynes, W. M. Physical Constants of Inorganic Compounds. In *CRC Handbook of Chemistry and Physics*, 97th ed.; CRC Press: Boca Raton, FL, 2016; p 4-43.
- (48) Benameur, M. M.; Radisavljevic, B.; Héron, J. S.; Sahoo, S.; Berger, H.; Kis, A. Visibility of Dichalcogenide Nanolayers. *Nanotechnology* **2011**, *22*, No. 125706.
- (49) Bertuch, A.; Sundaram, G.; Saly, M.; Moser, D.; Kanjolia, R. Atomic Layer Deposition of Molybdenum Oxide Using Bis(tert-Butylimido)bis(dimethylamido) Molybdenum. *J. Vac. Sci. Technol., A* **2014**, *32*, No. 01A119.
- (50) Miikkulainen, V.; Suvanto, M.; Pakkanen, T. A. Bis(tert-Butylimido)-Bis(dialkylamido) Complexes of Molybdenum as Atomic Layer Deposition (ALD) Precursors for Molybdenum Nitride: The Effect of the Alkyl Group. *Chem. Vap. Deposition* **2008**, *14*, 71–77.
- (51) Miikkulainen, V.; Suvanto, M.; Pakkanen, T. A. Atomic Layer Deposition of Molybdenum Nitride from Bis(tert-Butylimido)-Bis(dimethylamido)molybdenum and Ammonia onto Several Types of Substrate Materials with Equal Growth per Cycle. *Chem. Mater.* **2007**, *19*, 263–269.
- (52) Serna, M. L.; Yoo, S. H.; Moreno, S.; Xi, Y.; Oviedo, J. P.; Choi, H.; Alshareef, H. N.; Kim, M. J.; Minary-Jolandan, M.; Quevedo-Lopez, M. A. Large-Area Deposition of MoS<sub>2</sub> by Pulsed Laser Deposition with In Situ Thickness Control. *ACS Nano* **2016**, *10*, 6054–6061.
- (53) Li, H.; Zhang, Q.; Yap, C. C. R.; Tay, B. K.; Edwin, T. H. T.; Olivier, A.; Baillargeat, D. From Bulk to Monolayer MoS<sub>2</sub>: Evolution of Raman Scattering. *Adv. Funct. Mater.* **2012**, *22*, 1385–1390.
- (54) Li, S.-L.; Miyazaki, H.; Song, H.; Kuramochi, H.; Nakaharai, S.; Tsukagoshi, K. Quantitative Raman Spectrum and Reliable Thickness Identification for Atomic Layers on Insulating Substrates. *ACS Nano* **2012**, *6*, 7381–7388.
- (55) Eda, G.; Yamaguchi, H.; Voiry, D.; Fujita, T.; Chen, M.; Chhowalla, M. Photoluminescence from Chemically Exfoliated MoS<sub>2</sub>. *Nano Lett.* **2011**, *11*, 5111–5116.
- (56) Li, W.; Birdwell, A. G.; Amani, M.; Burke, R. A.; Ling, X.; Lee, Y.-H.; Liang, X.; Peng, L.; Richter, C. A.; Kong, J.; et al. Broadband Optical Properties of Large-Area Monolayer CVD Molybdenum Disulfide. *Phys. Rev. B: Condens. Matter Mater. Phys.* **2014**, *90*, No. 195434.
- (57) Park, J. W.; So, H. S.; Kim, S.; Choi, S.-H.; Lee, H.; Lee, J.; Lee, C.; Kim, Y. Optical Properties of Large-Area Ultrathin MoS<sub>2</sub> Films: Evolution from a Single Layer to Multilayers. *J. Appl. Phys.* **2014**, *116*, No. 183509.
- (58) Gao, J.; Li, B.; Tan, J.; Chow, P.; Lu, T.-M.; Koratkar, N. Aging of Transition Metal Dichalcogenide Monolayers. *ACS Nano* **2016**, *10*, 2628–2635.
- (59) *International Tables for Crystallography, Volume A: Space-Group Symmetry*, 1st ed.; Hahn, T., Ed.; International Union of Crystallography: Chester, U.K., 2006; DOI: [10.1107/97809553602060000100](https://doi.org/10.1107/97809553602060000100).
- (60) Schönfeld, B.; Huang, J. J.; Moss, S. C. Anisotropic Mean-Square Displacements (MSD) in Single-Crystals of 2H- and 3R-MoS<sub>2</sub>. *Acta Crystallogr., Sect. B: Struct. Sci.* **1983**, *39*, 404–407.
- (61) Wang, S.; Zhang, J.; He, D.; Zhang, Y.; Wang, L.; Xu, H.; Wen, X.; Ge, H.; Zhao, Y. Sulfur-Catalyzed Phase Transition in MoS<sub>2</sub> under High Pressure and Temperature. *J. Phys. Chem. Solids* **2014**, *75*, 100–104.
- (62) Addou, R.; Colombo, L.; Wallace, R. M. Surface Defects on Natural MoS<sub>2</sub>. *ACS Appl. Mater. Interfaces* **2015**, *7*, 11921–11929.
- (63) Baker, M. A.; Gilmore, R.; Lenardi, C.; Gissler, W. XPS Investigation of Preferential Sputtering of S from MoS<sub>2</sub> and Determination of MoS<sub>x</sub> Stoichiometry from Mo and S Peak Positions. *Appl. Surf. Sci.* **1999**, *150*, 255–262.
- (64) Zhu, H.; Qin, X.; Cheng, L.; Azcatl, A.; Kim, J.; Wallace, R. M. Remote Plasma Oxidation and Atomic Layer Etching of MoS<sub>2</sub>. *ACS Appl. Mater. Interfaces* **2016**, *8*, 19119–19126.
- (65) Fix, R.; Gordon, R. G.; Hoffman, D. M. Low-Temperature Atmospheric-Pressure Metal-Organic Chemical Vapor Deposition of Molybdenum Nitride Thin Films. *Thin Solid Films* **1996**, *288*, 116–119.
- (66) Estrade-Szwarckopf, H. XPS Photoemission in Carbonaceous Materials: A “defect” Peak beside the Graphitic Asymmetric Peak. *Carbon* **2004**, *42*, 1713–1721.
- (67) Jiang, Z.; Huang, W.; Zhang, Z.; Zhao, H.; Tan, D.; Bao, X. Thermal Decomposition of Mo(CO)<sub>6</sub> on Thin Al<sub>2</sub>O<sub>3</sub> Film: A Combinatorial Investigation by XPS and UPS. *Surf. Sci.* **2007**, *601*, 844–851.
- (68) Hofmann, W. K. Thin Films of Molybdenum and Tungsten Disulphides by Metal Organic Chemical Vapour Deposition. *J. Mater. Sci.* **1988**, *23*, 3981–3986.

## Supporting Information

### Rapid Wafer-Scale Growth of Polycrystalline 2H-MoS<sub>2</sub> by Pulsed Metalorganic Chemical Vapor Deposition

*Berc Kalanyan<sup>†</sup>, William A. Kimes<sup>†</sup>, Ryan Beams<sup>†</sup>, Stephan J. Stranick<sup>†</sup>, Elias Garratt<sup>†</sup>, Irina Kalish<sup>†</sup>,  
Albert V. Davydov<sup>†</sup>, Ravindra K. Kanjolia<sup>‡</sup>, James E. Maslar<sup>†</sup>*

<sup>†</sup>Materials Measurement Laboratory, National Institute of Standards and Technology,  
Gaithersburg, Maryland 20899, United States;

<sup>‡</sup>EMD Performance Materials, Haverhill, Massachusetts 01835, United States.

#### Growth Temperature

Growth temperature is expected to be the strongest parameter affecting film quality. To study the influence of process temperature on film crystallinity, we compared XRD patterns obtained from films grown at temperatures ranging from 351 °C to 591 °C. Growth at 351 °C resulted in films that were <8 nm thick (inferred from presence of Si 2p transitions in XPS spectra), which is too thin for conventional XRD analysis. Films grown at  $\geq 400$  °C were thick enough to exhibit new reflections in addition to those associated with the substrate. It is evident from Figure S1 that degree of film's crystallinity is dependent on the growth temperature as the full width at half maximum (FWHM) of the (000 $l$ ) family of peaks decreases and d-spacing (c-lattice parameter) decreases with temperature, approaching the values reported in the literature. As expected, the higher index (000 $l$ ) peaks exhibit a larger degree of broadening. Note that growth rate also increases with temperature.

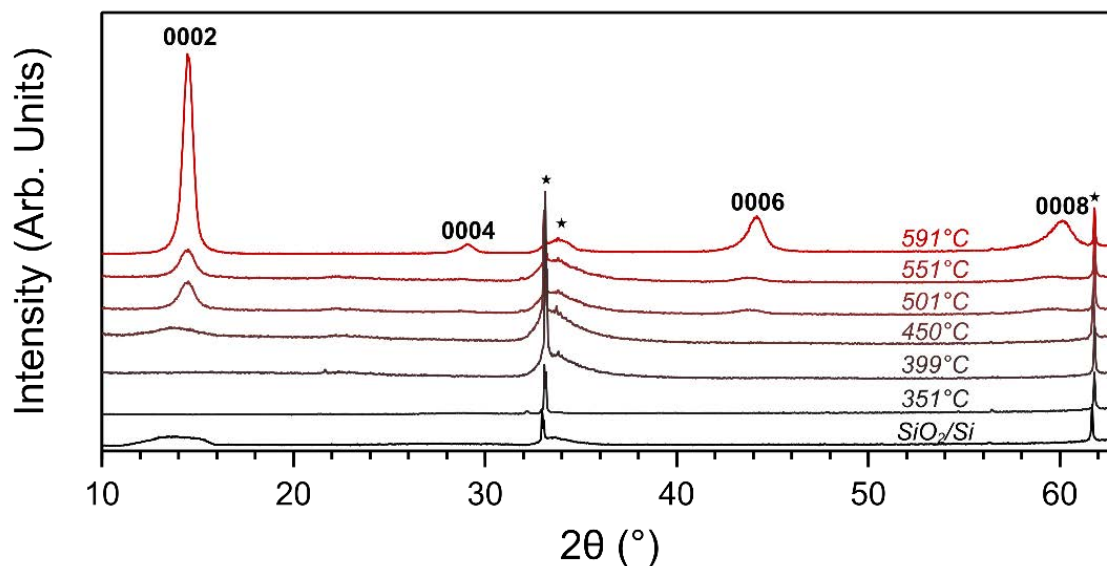


Figure S1. XRD of films ( $n=200$ ) grown at various substrate temperatures. Reflections identified with a star (★) denote substrate peaks.

Peak positions and assignments for the XRD measurements are listed in the following table:

Table S1. Positions and assignments for MoS<sub>2</sub> peaks from XRD measurement on a film grown with  $n=200$  at 591 °C.

<b>2θ (°)</b>	<b>Assignment</b>
14.46	MoS <sub>2</sub> (0002)
29.06	MoS <sub>2</sub> (0004)
44.18	MoS <sub>2</sub> (0006)
60.140	MoS <sub>2</sub> (0008)

## Onset of Film Nucleation

High resolution XPS spectra that capture the early nucleation of MOCVD films are shown in Figure S2. The Mo 3d region for a film grown with one injection of precursors ( $n=1$ )

clearly shows a Mo 3d doublet assigned to oxidized Mo. The signal to noise ratio is not high enough to discern any additional peaks. After three injections ( $n=3$ ), a lower binding energy doublet assigned to MoS<sub>2</sub> emerges, alongside the corresponding S 2s peak. The presence of Mo on the surface even after one injection indicates that the incubation time on the SiO<sub>2</sub> surface is negligible for our MOCVD process under the conditions examined.

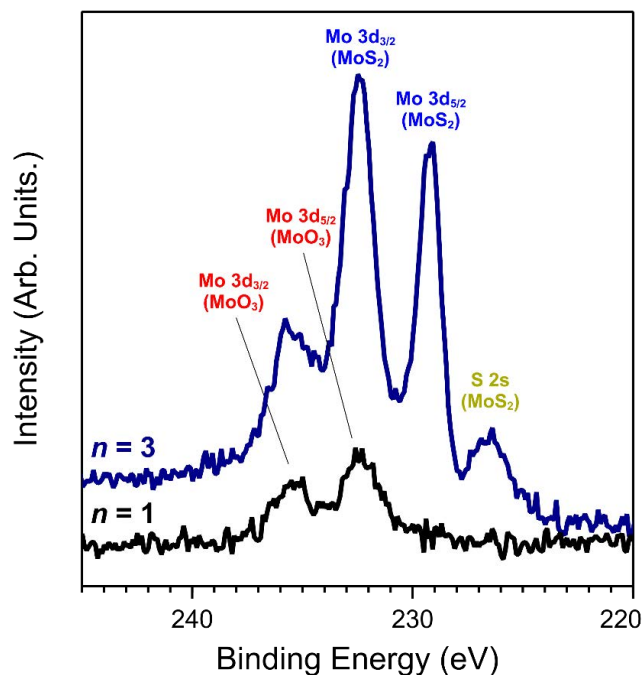


Figure S2. High resolution XPS spectra from films grown using  $n=1$  and  $n=3$  showing the early onset of Mo 3d and S 2s peaks.

## Film Topography and Roughness

Topographic AFM maps of the MOCVD grown films are presented in Figure S3 for the full set of film thicknesses ( $n=1$  to  $n=200$ ) explored in this study. Measurements for  $n=50$  and  $n=100$  show distinct tall features that correspond with surface roughness also observed in SEM images in Figure 4 and Figure S4.

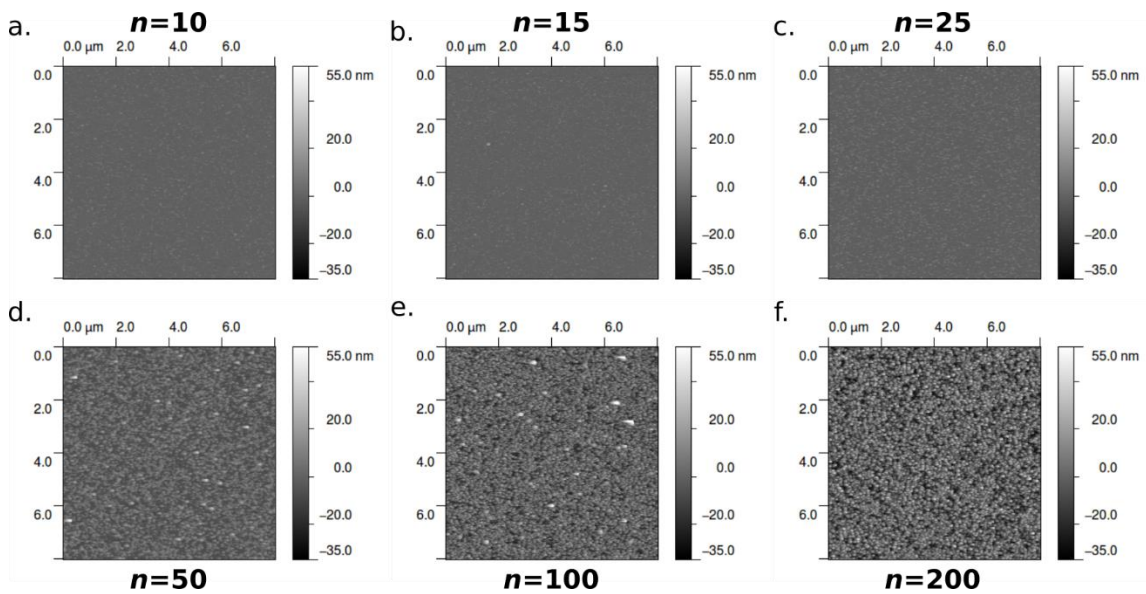


Figure S3. AFM topographic scans for (a)  $n=10$ , (b) 15, (c) 25, (d) 50, (e) 100, and (f) 200.

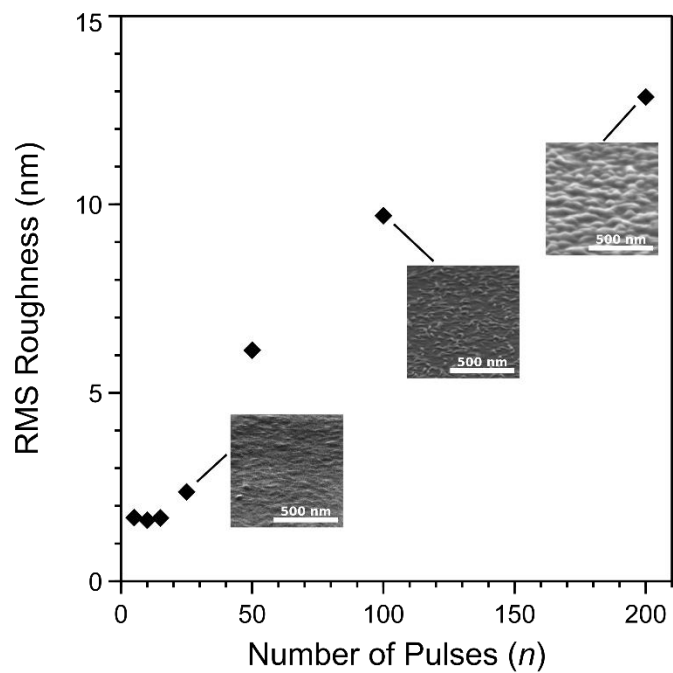


Figure S4. RMS roughness vs  $n$ , with accompanying SEM images

## Thickness Determination from XPS

Thickness estimation using XPS relies on the calculation of an inelastic mean free path (IMFP) value ( $\lambda$ ) for Si 2p photoelectrons originating within the SiO<sub>2</sub>/Si substrate. The IMFP estimate based on the TPP-2M method<sup>1</sup> is implicitly dependent upon the composition of the thin film overlayer, since  $\lambda$  is a function of density, valence electron count, and band gap. Given that our MOCVD films contain carbon residue and a MoO<sub>3</sub> native oxide, we considered the sensitivity of  $\lambda$  to film composition. The thickness of the native oxide is expected to have a negligible contribution to the thickness calculation, since Si 2p attenuation from MoS<sub>2</sub> and MoO<sub>3</sub> overlayers are nearly equivalent, with  $\lambda_{MoO_3} = 2.512$  and  $\lambda_{MoS_2} = 2.465$  nm. Carbon, however, is about 1.3 times less attenuating than either MoS<sub>2</sub> or MoO<sub>3</sub> ( $\lambda_{carbon}=3.364$  nm for 1383 eV electrons). Therefore, depending on fractional carbon content, our thickness estimate from Si 2p attenuation may underreport MoS<sub>2</sub> thickness by approximately 30%. Regardless of the absolute IMFP value used in this analysis, the trends observed in the thickness estimate (Figure 4 in the main text) are valid.

Overlayer thickness was calculated using the following expression<sup>2</sup>:

$$t_{MoS_2} = -\lambda_{MoS_2} \ln(A_{Si\ 2p}/A_{Si\ 2p,0})$$

Where  $t_{MoS_2}$  is the overlayer thickness in nm,  $\lambda_{MoS_2}$  is the IMFP for the overlayer,  $A_{Si\ 2p,0}$  is the initial Si 2p peak area for a bare substrate, and  $A_{Si\ 2p}$  is the Si 2p peak area after film growth. The initial substrate peak area ( $A_{Si\ 2p,0}$ ) was not measured directly, since atmospheric contamination and its subsequent transformation in the reactor could not be excluded. Rather than directly measuring  $A_{Si\ 2p,0}$ , we generated the MoS<sub>2</sub> thickness curve by choosing the initial Si 2p area such that the XPS estimate at  $n=25$  coincided with the cross-

sectional HRTEM measurement obtained from the same surface. This amounts to a single-point calibration against the TEM measurement and effectively introduces a y-offset. Similar to the composition-dependent uncertainty in IMFP, discussed in the previous paragraph, the y-offset does not modify in any way the linear trend observed in Figure 4 and the growth rate that was subsequently calculated.

### **Compositional Analysis by XPS Depth Profiling**

XPS depth profiling was used to remove carbonaceous material from the surface of a thick MoS<sub>2</sub> film. At short sputter times ( $\leq 1$  min), we removed the top few nm of material in order to eliminate contributions to the overall film composition from atmospheric contamination. The film was  $\approx 25$  nm in thickness (assuming a linear growth rate), which ensured that all emitted photoelectrons originated from within the film, rather than the substrate. Such a depth profile from a film grown using  $n=200$  is shown in Figure S5. Composition values were calculated using the peak areas for the O 1s, C 1s, Mo 3d, and S 2p regions. Nitrogen was not detected in these films. Relative sensitivity factors were provided by the instrument manufacturer (Kratos Analytical) and were used as given in the CasaXPS software package.

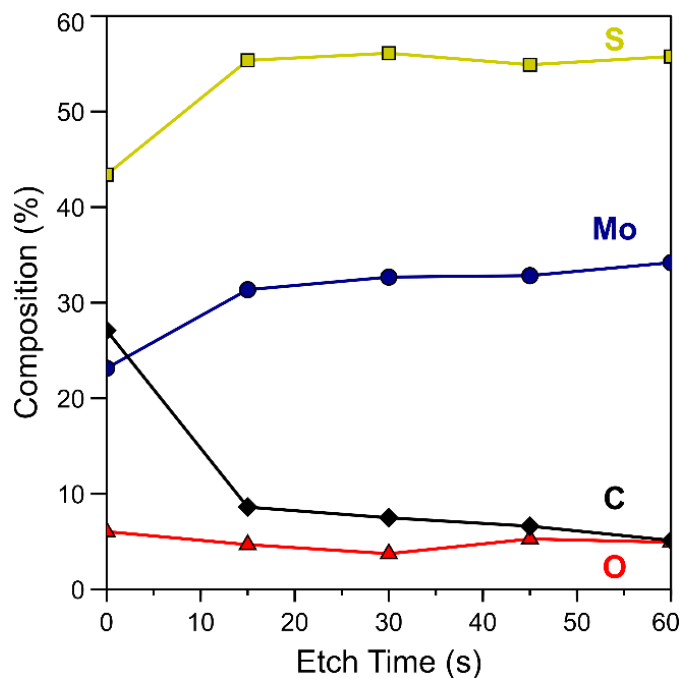
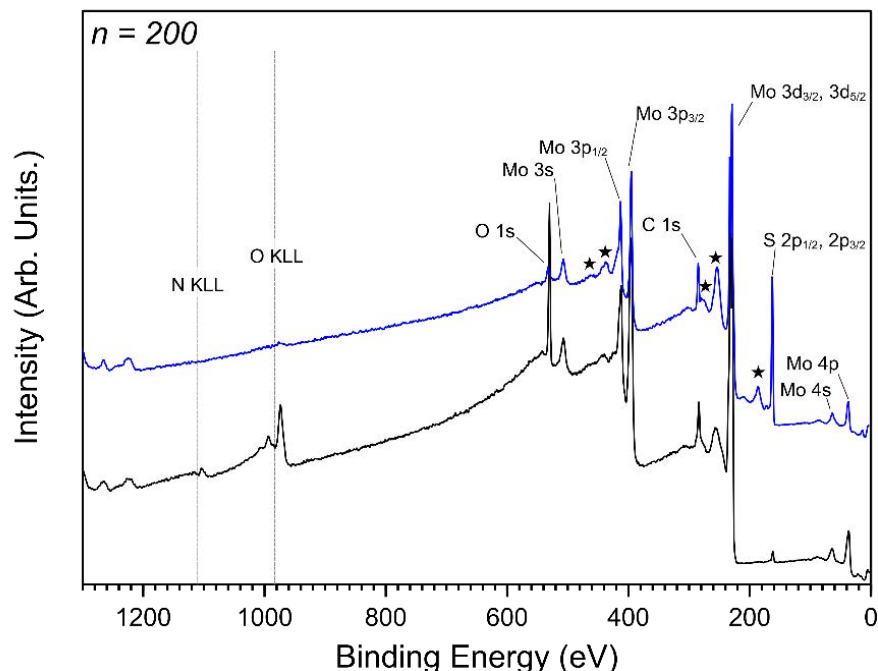


Figure S5. XPS depth profile of a thick MoS<sub>2</sub> specimen ( $n=200$ ) using a 4 keV Ar<sup>+</sup> ion beam.

### XPS Survey Scans for Films Grown with and without Et<sub>2</sub>S<sub>2</sub>

Survey scans from two sets of thick films growth with and without Et<sub>2</sub>S<sub>2</sub> are shown in Figure S6. These complement the high resolution scans discussed in the main text and also shown in Figure 7. The notable feature in the survey scans is the presence of the N KLL transition for the film grown without Et<sub>2</sub>S<sub>2</sub>, which supports the interpretation of the Mo 3d region and the assignment of the N 1s feature.



*Figure S6.* Survey scans from films grown using  $(\text{N}^t\text{Bu})_2(\text{NMe}_2)_2\text{Mo}$  only (black trace) and those grown using the Mo source and  $\text{Et}_2\text{S}_2$  (blue trace). Positions of the N and O Auger transitions are marked with dashed lines. Features identified with a star (★) are generally associated with  $\text{MoS}_2$ , including plasmon peaks.

## Wafer-Scale Uniformity

To investigate film uniformity on 50 mm diameter substrates, one of the fused quartz wafers shown in Figure 2 in the main text was measured using XPS. Spectra from the Si 2p core level region were recorded for 8 distinct points at 5 mm intervals along the centerline of the wafer. The edges of the wafer were omitted to exclude signal from the sample clips. Film thickness was calculated using Si 2p attenuation as described above, assuming an  $\text{MoS}_2$  overlayer. An uncoated quartz wafer was used as a reference. For a film grown using 15 injections ( $n = 15$ ), coating thickness was estimated at 3.9 nm with a standard deviation of 0.1 nm for the  $\approx 35$  mm long region sampled. Note that film thickness on fused quartz is larger than

on thermal SiO<sub>2</sub>/Si, which could be explained by differences between the two substrates. While the thermally oxidized Si wafers are expected to have smooth surfaces, the polished silica wafers we used for this demonstration are not semiconductor grade substrates and therefore do not have roughness specifications. Since the XPS measurement does not account for morphology, attenuation of the substrate signal and the calculated film thickness will depend on roughness. Surface temperatures during growth are also likely to be different due to emissivity differences between the two substrates.

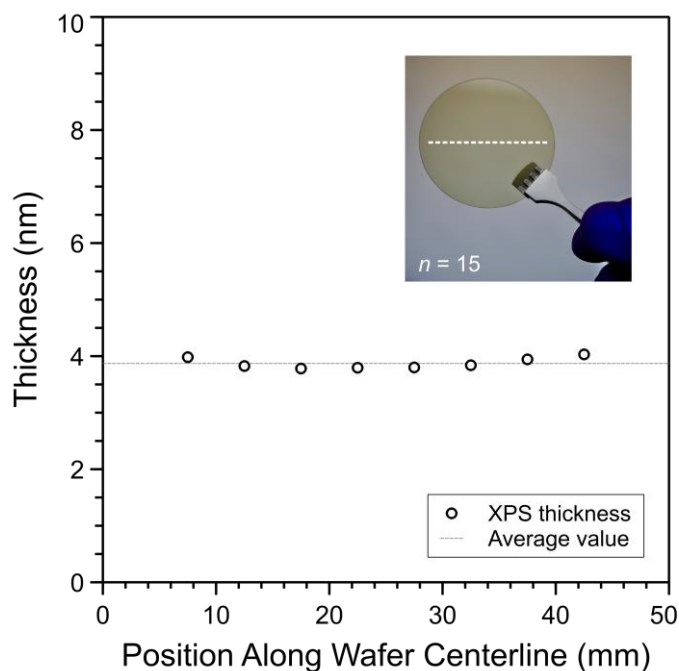


*Figure S7.* Thickness profile from a 50 mm fused quartz wafer coated using 15 injections ( $n = 15$ ) of (N<sup>t</sup>Bu)<sub>2</sub>(NMe<sub>2</sub>)<sub>2</sub>Mo and Et<sub>2</sub>S<sub>2</sub> at nominally 591 °C. Film thickness values are calculated by XPS. The dashed line in the inset denotes the approximate region from which individual spots were measured.

## XPS Data Processing and Peak Fitting

High resolution XPS data were modeled using synthetic peak shapes as provided by the CasaXPS v2.3.17 software package. Line shapes defined as GL were a mixture of Gaussian and Lorentzian components. Those termed as A denote a modified Voigt function. Those termed as LA denote an asymmetric Lorentzian function. Background types were Shirley or linear, depending on the region. Binding energy correction was done based on the S 2p<sub>3/2</sub> peak (S-Mo, 226.3 eV<sup>3</sup>) assigned to MoS<sub>2</sub>. We used S 2p because the composition of the C 1s region changed based on the deposition chemistry, *i.e.* growths done with and without Et<sub>2</sub>S<sub>2</sub> showed distinct changes in the carbon spectra and the C-H peak typically used for charge calibration could not be reliably identified. Conveniently, S 2p<sub>3/2</sub> could be used as a stable reference point for all measurements because residual sulfur in the reactor produced a small amount of MoS<sub>2</sub> even in the growth runs conducted without Et<sub>2</sub>S<sub>2</sub> injections.

*Table S2.* Peak assignments, positions, shapes, and fitting constraints used in the XPS analyses for films grown with and without Et<sub>2</sub>S<sub>2</sub>.

<b>Transition</b>	<b>Position (eV)</b>	<b>Assignment</b>	<b>Peak Shape</b>	<b>Constraints</b>
Mo 3p	417.4	Plasmon	GL(30)	None
Mo 3p <sub>3/2</sub>	399.0	MoO <sub>3</sub>	GL(50)	None
Mo 3p <sub>1/2</sub>	416.5	MoO <sub>3</sub>	GL(50)	Area, position
Mo 3p <sub>3/2</sub>	395.0	MoS <sub>2</sub>	GL(50)	None
Mo 3p <sub>1/2</sub>	412.5	MoS <sub>2</sub>	GL(50)	Area, position
N 1s	397.8	Mo <sub>x</sub> N <sub>y</sub>	GL(90)	None
C 1s	284.2	Graphitic carbon	A(0.29,0.61,0)GL(0)	None
C 1s	284.5	C-H	GL(30)	FWHM
C 1s	286.6	C-O	GL(30)	FWHM
C 1s	288.6	C=O or C-N	GL(30)	FWHM
Mo 3d <sub>5/2</sub>	229.1	MoS <sub>2</sub>	LA(2.9,4,6)	None
Mo 3d <sub>3/2</sub>	232.3	MoS <sub>2</sub>	LA(2.9,4,6)	Area
Mo 3d <sub>5/2</sub>	232.5	MoO <sub>3</sub>	GL(50)	FWHM, position
Mo 3d <sub>3/2</sub>	235.6	MoO <sub>3</sub>	GL(50)	None
Mo 3d <sub>5/2</sub>	228.9	Mo <sub>x</sub> N <sub>y</sub>	LA(1.35,5,6)	None

Mo 3d <sub>3/2</sub>	232.1	Mo <sub>x</sub> N <sub>y</sub>	LA(1.35,5,6)	Area
S 2s	226.4	MoS <sub>2</sub>	GL(90)	None
S 2p <sub>3/2</sub>	162.0	MoS <sub>2</sub>	GL(50)	None
S 2p <sub>1/2</sub>	163.2	MoS <sub>2</sub>	GL(50)	Area
Si 2s	154.4	SiO <sub>2</sub>	GL(30)	None
Si 2p	103.7	SiO <sub>2</sub>	GL(30)	None

## REFERENCES

- (1) Powell, C. J.; Jablonski, A. *J. Phys. Chem. Ref. Data* **1999**, *28* (1), 19–62.
- (2) Mitchell, D. F.; Clark, K. B.; Bardwell, J. A.; Lennard, W. N.; Massoumi, G. R.; Mitchell, I. V. *Surf. Interface Anal.* **1994**, *21* (1), 44–50.
- (3) Ganta, D.; Sinha, S.; Haasch, R. T. *Surf. Sci. Spectra* **2014**, *21* (1), 19–27.